



# Numerical modelling of reservoir at pore scale: A comprehensive review

Yuzhu Wang<sup>a,\*</sup>, Sheik S. Rahman<sup>b</sup>

<sup>a</sup> Department of Petroleum Engineering, CPG, King Fahd University of Petroleum and Minerals, Dhahran, 31261, Saudi Arabia

<sup>b</sup> School of Minerals and Energy Resources Engineering (MERE), Faculty of Engineering, University of New South Wales (UNSW), Sydney, Australia

## ARTICLE INFO

### Article history:

Received 18 September 2019

Received in revised form 20 September 2022

Accepted 4 October 2022

Available online 7 October 2022

### Keywords:

Porous structure reconstruction

Numerical modelling

Reservoir characterization

## ABSTRACT

Pore scale reservoir modelling is carried out to digitally build the inner structure of the reservoir samples using proper mathematical algorithms based on certain priors extracted from training image(s) or laboratory measured data. Although various imaging devices can provide the inner structure of the rock sample directly, numerical modelling methods still has its irreplaceable advantages. Firstly, due to some intrinsic limitations, no imaging device so far can provide a 3D porous structure satisfying both resolution and field of view except for a very few of homogeneous reservoir samples with relatively large pore-throat size, while numerical modelling is an effective approach to improve the resolution of the machine produced images. Secondly, in some cases, where only 2D images (such as the images of drill cuttings) are available, numerical modelling is the only option to reconstruct a 3D porous structure. Thirdly, numerical modelling is a convenient and low-cost technique that makes it widely applicable. This paper presents a comprehensive review of the pore scale reservoir modelling. Pore structure's modelling can be treated as a supervised prediction process with two steps: 1) extraction of descriptors (prior knowledge) from the training image(s) or laboratory measured data; and 2) numerical reconstruction under the supervision of the extracted descriptors. In terms of extraction of descriptors, using multiple-point statistics (MPS) instead of random function models is a great step that made the empirical multivariate distributions inferred from training images can be directly used to reconstruct porous structure. Another great progress is the application of multiple-resolution training images where the image degradation mechanism contained in these different resolution images can be used to supervise the reconstruction. In terms of supervised reconstruction, some mathematical strategies such as Gaussian Random field, simulated annealing are applied to reproduce these descriptors in the reconstructed images. Along with the flourish of deep learning, a convolutional neural networks model is introduced into reconstruction process with an impressive performance.

© 2022 Elsevier Inc. All rights reserved.

## 1. Introduction

A high-quality three-dimensional (3D) porous structure is the premise to quantitatively evaluate the transport properties of reservoirs at pore scale. Prior to the universal use of micro X-ray computed tomography ( $\mu$ -CT) and focused ion beam

\* Corresponding author.

E-mail address: [yuzhu.wang@kfupm.edu.sa](mailto:yuzhu.wang@kfupm.edu.sa) (Y. Wang).

scanning electron microscopy (FIBSEM), numerical modelling was the only choice to obtain a 3D digital porous structure. The prior knowledge (e.g., two-point probability function and lineal-path function) is firstly extracted from 2D sections (e.g., scanning electron microscope (SEM) and optical microscope image(s)) or experimental data (e.g., grain size distribution), and then a certain of mathematical frame work (e.g., Gaussian random field) is selected to estimate the phase of each voxel based on the extracted prior. Currently, this 2D to 3D reconstruction method still has irreplaceable applications in petroleum industry. For example, in some situations where the well cores are unavailable, drill cuttings can be collected and be consolidated in resin and scanned by SEM to get a set of 2D images [1–3]. Then the 3D porous structure can be constructed using numerical modelling method based on these 2D images. This method also has an extra advantage that is the drill cutting can be continuously collected along the entire wellbore rather than a certain well sections where well cores are extracted. Another important utility of this 2D to 3D reconstruction comes from multiscale pore structure modelling which is used to build highly heterogeneous rock samples such as limestones, tight sandstones and shales. For example,  $\mu$ -CT image can be used to observe the spatial distribution of the clay and kerogen of a shale sample, but is insufficient to detect the nanoscale pore structures inside the kerogen and clay. These nanoscale structures inside the kerogen and clay can be described by high-resolution 2D SEM images [4,5]. Therefore, a multiscale pore structure reconstruction strategy can be applied to describe the pore structure of shale samples with two steps: 1)  $\mu$ -CT image is used to characterize the microscale features; and 2) for special facies, such as clay and kerogen [6], numerical modelling method is applied to reconstruct its inner nanoscale structures based on 2D SEM images [7].

Pore scale numerical modelling method also plays an important role in improving the rock sample images' resolution. The highest resolution of the rock samples'  $\mu$ -CT images is about several millimetres (say 2 microns) [8–10], which is insufficient to characterize some small structures of the reservoir rocks, such as tiny throats and sub-micro scale pores. Besides, the sample size of the  $\mu$ -CT image with 2  $\mu$ m resolution is always extremely small (say a 5 mm diameter cylinder with 5 mm length). These small structures are critical for the properties of fluid transportation in porous media. Focused ion beam scanning electron microscopy (FIB/SEM) is another choice for generating 3D imaging of porous structure and its resolution reaches a few nanometres, however, its field of view (FOV) is limited within several micrometres which is too local to cover the heterogeneity of most rock samples [11]. The foregoing drawbacks can be significantly relieved by the numerical method.

Most pore scale numerical modelling methods are originated from reservoir-scale modelling, namely geostatistics. 3D pore scale numerical modelling of reservoir rocks dates back to 1984 when Quiblier generated a 3D-porous structure using the characteristics properties derived from 2D thin sections [12]. His method is to successively pass a normalized uncorrelated Gaussian random field through a linear and then a nonlinear filter to generate a pore structure image [13]. This filtering method is quite general [14] but robust [15] and has been used universally in modelling various porous media range from food to rock samples [9,16–20]. However, the utility of one- and two-point probability functions have been found insufficient to reproduce the pore connectivity of a complex porous structures [13]. The Gaussian filtering reconstruction methods retain a similar degree of isotropy and homogeneity as original training image but cannot reproduce connectivity which are critical for transport properties of rocks [21]. In order to overcome this issue, some morphological descriptors that contain information related to pore connectivity are introduced to constrain reconstruction process. Some typical constrains are (1) two-point cluster function, (2) lineal-path length and (3) chord-length function.

Because it is difficulty to incorporate these new descriptors into the aforementioned filtering method, simulated annealing (SA) was proposed to reconstruct porous media subject to various statistical constrains [13,22–24]. SA algorithm allows arbitrary structural descriptors imported into the reconstruction procedure as constrains, which improve the accuracy of modelling. Although this method has been successfully used to reconstruct several materials, including sandstone [25] and chalk [26], the resulting images do not always capture the long-range connectivity of pores, namely the low porous materials. It is difficult to obtain a global minimum for these low porosity media and therefore, can only be used in reconstructing some specific media [27]. In addition, the tedious computation, involved in SA modelling, is another obstacle for its application to numerical modelling of porous structure.

Another innovative approach of pore structure modelling method is the process-based reconstruction which numerically mimics the geological process of the forming of sedimentary rocks [28–31]. An essential precondition for use of this method is understanding of the physical and chemical processes of formation of the porous structure which is always difficult to be pursued [32], especially for carbonates and shale gas reservoirs.

Wu et al., [33] proposed an effective method to generate the pore structures in 2D by replicating patterns in a five-point stencil using a Markov chain Monte Carlo method. This algorithm was extended to model 3D porous structure in their subsequent work by using three 2D training sections that perpendicular with each other. These three sections are used to extract prior to determine the transition probabilities controlling the following reconstruction process which can be treated as a Markov chain process. MCMC algorithm was soon generalized to multiple-point statistics (MPS) method by Okabe and Blunt [34]. Later, they extended their work to recover the small features lost in low resolution  $\mu$ -CT image by combining 2D SEM images with 3D low resolution  $\mu$ -CT image [35]. In their approach, macro-pores are identified by  $\mu$ -CT while micro-pores that is lost in the  $\mu$ -CT image are supplemented by MPS reconstruction method based on SEM image. In theory, it is possible to reproduce the porous structure perfectly if the template size is large enough and training image can provide sufficient number of replicas for actual data event. However, due to the limitation of CPU, RAM and training image size, the challenge of reproducing the long-range connectivity is yet to be overcome. Along with the development of deep learning, some neural networks reconstruction methods are proposed to reconstruct high resolution porous structure. Mosser et

al., [36] proposed a generative adversarial networks (GAN) reconstruction method to reconstruct an oolitic limestone. A convolutional neural networks reconstruction (CNNR) method is proposed by Wang, et al. [37] to build a high-resolution porous structure based on low-resolution  $\mu$ -CT image and high-resolution SEM image(s). This algorithm integrates the super resolution and segmentation processes. The input data are low-resolution tomographic  $\mu$ -CT images, and the output data are high-resolution segmented porous structures.

Over the past half century, pore scale reservoir modelling has been developed to be a large family consisting of diverse reconstruction methods. In general, the numerical modelling of porous structure is a supervised prediction technique with two steps: 1) extraction of descriptors (prior knowledge) from training image(s) or experiment data, and 2) numerical reconstruction under the supervision of the extracted descriptors applying proper mathematical strategies. Porous structure reconstruction methods can be divided into four categories according to the descriptors: experiment data, two-point correlation functions, multiple-point statistics and multiple-resolution training images. According to the mathematical strategies, these methods can be divided into five classes, Poisson distribution reconstruction, Gaussian random field reconstruction, simulated annealing reconstruction, Markov random field reconstruction and convolutional neural networks reconstruction. In this paper, the first classification criterion is applied to review these methods in details.

## 2. Pore scale numerical modelling

### 2.1. Reconstruction using experiment data

Porous structure reconstruction using experiment data as constrains is also known as process-based reconstruction. Different from conventional voxel-based reconstruction methods, where the structure model is estimated voxel by voxel, process-based modelling estimates an object (a group of voxels with specific shape and size) for every iteration step. Thus, process-based reconstruction belongs to object-based reconstruction method. The input data of process-based reconstruction method is some structural parameters such as porosity, grain-size distribution, grain-shape factor (define the shape of grains) which can be obtained from laboratory measurements. Process-based reconstruction method numerically mimics the geological process of the forming of sedimentary rocks. This idea is pioneered by Bryant and Blunt [29] through packing together large number of equally-sized spheres as initial deposited grains. Then, compaction process is considered by moving the centres of these spheres closer in vertical direction. Another important process of the rock forming is diagenesis which is modelled by swelling the spheres uniformly. Both compression and diagenesis process allow spheres overlap with each other.

This method was improved by Bakke and Øren [38] via selecting individual grains from a given grain-size distribution which is closer to the natural circumstances. In addition, they considered the energy of sedimentary environment to decide the location of single grain deposit on the grainbed. Low-energy sedimentation results in fine grain deposition such as silty sandstone and mudstone. In this case, each new randomly selected grain is dropped onto the grainbed and then roll into a local stable position (local minimum). However, in high-energy environment, the lateral force loaded by streams and waves causes the new selected grain to be placed at the lowest available position (global minimum) in the grainbed. In order to deal with the location problem for unequal size grains, an ingenious method is proposed by Bryant and Blunt [29]. Before a new grain, whose radius is  $r$ , deposits on the existing grainbed, its radius reduces to zero (grain point) but the radius of all the grains in grainbed increase by an amount  $r$ . The radius increased grainbed generates a new fictitious solid surface, a surface which is shifted by the radius of the new grain. Once the new grain finds its final position (local- or global-minimum) on the grainbed, the radius of all grains including new grain and grainbed grains are reset to their original value. Compaction and diagenesis was modelled in a similar manner to that presented by Bryant and Blunt [29]. Clay particles are also considered in this model.

Furtherly, Coelho, Thovert and Adler [30] extended this work to simulate the deposition of grains using aspherical particles. Later Latham, Lu and Munjiza [31] applied tetrahedral to simulate loose packs of particles. These non-spherical shapes extended the use of process-based method.

Process-based reconstruction has two main advantages. Firstly, it runs fast due to the pore structure is built grain by grain rather than voxel by voxel. Secondly, it has been proven to be highly effective in reproducing some intrinsic properties in sandstone. For example, Øren and Bakke [28] applied process-based method to reconstruct the Fontainebleau sandstone and compared quantitatively the structure properties of the reconstructed structure with that of the reference image obtained from the  $\mu$ -CT images. It shows that process-based method reproduced some important intrinsic properties, such as connectivity, specific internal surface and two-point correlation function. However, the geological process of porous media formation is extremely complex and therefore, numerical simulation of geological formation is a difficult task, especially for some rocks which are affected greatly by diagenesis or have poor sorting.

### 2.2. Reconstruction using two-point correlation functions

Two-point correlation functions define the probability of the existing of two voxels with a departure of  $\vec{r}$  have same phase. The most common two-point correlation functions are variogram and two-point probability function (a variant of the variogram). Because variogram fails to describe the connection information between these two points, other stricter two-point correlation functions including two-point cluster function, lineal-path function and chord-length function are

proposed to supplement connection information into the descriptors. According to the mathematical models used in the reconstruction, two-point correlation function based reconstruction can be divided into two categories: Gaussian random field reconstruction and simulated annealing reconstruction.

#### Gaussian random field based reconstruction (GRFR)

Gaussian random fields (GRF) is used universally in porous structure reconstruction for two main reasons: 1) the specification of its finite-dimensional distribution is simple; and 2) its mathematical formulation is reasonable for describing many natural phenomenon and estimation [39]. A GRF is a random field where all the finite-dimensional distributions,  $F_{r_1, \dots, r_k}$ , are multivariate Gaussian distributions for any choice of  $k$  and  $\{r_1, \dots, r_k\}$  [39]. The porous structure reconstruction based on GRF is originally developed in two-dimensions by Joshi [40] and then extended to three-dimensions by Qubilier [12] and Adler [41]. Therefore, it is also called the JQA model [42]. The simulation is carried out via following operations.

Firstly, calculate the reference two-point probability function from training 2D image,  $T$ . Here,  $T$  is a binary image contains two phases, 0 for solid and 1 for void. Bron and Jeulin [20] used covariance as two-point probability function as follows:

$$\text{Cov}(\vec{h}) = \text{Cov}[T(\vec{r}), T(\vec{r} + \vec{h})] = \frac{1}{MN} \text{FFT}^{-1}(\text{FFT}(T) \times \overline{\text{FFT}(T)}) - \emptyset^2 \quad (1)$$

where  $\vec{r}$  denotes any pixel of training image  $T$ , and  $\vec{h}$  is a translation vector defining the distance and direction between two points.  $E[\cdot]$  is calculating expectation.  $M$  and  $N$  are numbers of rows and columns of image  $T$ .  $\text{FFT}$  and  $\text{FFT}^{-1}$  represent fast Fourier transform and inverse fast Fourier transform respectively.  $\bar{x}$  is the conjugate of  $x$ .  $\emptyset$  is the porosity. The “physical meaning” of function,  $\text{Cov}(\vec{h})$  is the probability of the two points departed by vector  $\vec{h}$  and these two points belong to void.

Then, generate a cubic domain,  $D$  and give every position,  $\vec{r} \in D$  a random number  $U(\vec{r})$  and all of these numbers constitute a standard Gaussian population with 0 mean and 1 variance:

$$\forall \vec{r} \in D, U(\vec{r}) \sim N(0, 1) \quad (2)$$

It is obvious that the generated Gaussian random field  $U(\vec{r})$  is completely uncorrelated ( $\text{Cov}[U(\vec{r}_i), U(\vec{r}_j)] = 0, i \neq j$ ). In order to reconstruct a realistic porous structure, a correlation is imposed by convolving  $U(\vec{r})$  with a linear-filter  $w$ :

$$Z(\vec{r}) = (U * w)(\vec{r}) \quad (3)$$

where  $w$  has to satisfy two conditions, normalized and symmetric as shown in Eq. (12).

$$\begin{cases} \sum_{\vec{r} \in \Omega} w^2(\vec{h}) = 1 \\ \forall \vec{r} \in \Omega, w(-\vec{r}) = w(\vec{r}) \end{cases} \quad (4)$$

The proof of these two features refers to appendix. Then the reconstructed image  $Z$  has two important features:

$$\begin{aligned} \forall \vec{r} \in \Omega, Z(\vec{r}) &\sim N(0, 1) \text{ and} \\ \text{Cov}[Z(\vec{r}), Z(\vec{r} + \vec{h})] &= (w * w)(\vec{h}) \end{aligned} \quad (5)$$

Next, image  $Z$  is segmented by setting a threshold  $\mathcal{E}$  to get the binary simulation  $B$ :

$$B(\vec{r}) = \begin{cases} 1, & \text{if } Z(\vec{r}) \geq \mathcal{E} \\ 0, & \text{if } Z(\vec{r}) < \mathcal{E} \end{cases} \quad (6)$$

Where threshold  $\mathcal{E}$  is given by:

$$\mathcal{E} = C^{-1}(1 - \emptyset) \quad (7)$$

Where  $C$  is the cumulative distribution function of a standard Gaussian and  $C^{-1}$  is the inverse function of  $C$ ,  $\emptyset$  is porosity.

Then, random variable  $(Z(\vec{r}), Z(\vec{r} + \vec{h}))$  can be defined as a bivariate Gaussian distribution [20]:

$$g(z_1, z_2, \rho) = \frac{1}{2\pi\sqrt{1-\rho^2}} e^{-\frac{z_1^2 + z_2^2 - 2\rho z_1 z_2}{2(1-\rho^2)}} \quad (8)$$

Where  $z_1$  and  $z_2$  represent  $Z(\vec{r})$  and  $Z(\vec{r} + \vec{h})$  respectively, and  $\rho$  is similarity coefficient between  $Z(\vec{r})$  and  $Z(\vec{r} + \vec{h})$ . Because segmented image,  $B(\vec{r})$  has the same two-point probability function as training image,  $T(\vec{r})$ , the following equation can be obtained:

$$\int_{\varepsilon}^{+\infty} \int_{\varepsilon}^{+\infty} g(z_1, z_2, \rho) dz_1 dz_2 = \text{Cov}(\vec{h}) \quad (9)$$

where the left-hand terms of Eq. (9) can be defined as the probability of both two points departing from each other by  $\vec{h}$  and these two points are in void phase of the reconstructed image,  $B(\vec{r})$  and right item has the same meaning of training image,  $T(\vec{r})$ . After integration, left item just contains one variable,  $\rho$  which can be inversed. According the definition of similarity coefficient:

$$\rho(\vec{h}) = \frac{\text{Cov}[Z(\vec{r})Z(\vec{r} + \vec{h})]}{\sqrt{\text{var}[Z(\vec{r})]\text{var}[Z(\vec{r} + \vec{h})]}} = \text{Cov}[Z(\vec{r}), Z(\vec{r} + \vec{h})] \quad (10)$$

where  $\text{Cov}[Z(\vec{r}), Z(\vec{r} + \vec{h})]$  is the two-point probability function as defined earlier. Therefore, according Eq. (5) and Eq. (10),

$$(w * w)(\vec{h}) = \rho(\vec{h}) \quad (11)$$

And then  $w(\vec{h})$  can be solved by:

$$w(\vec{h}) = \text{FFT}^{-1}(\sqrt{\text{FFT}(\rho(\vec{h}))}) \quad (12)$$

Once  $w(\vec{h})$  is obtained, Eq. (3) can be used to generate the non-conditional Gaussian random realization. Then, this realisation can be segmented to binary image by Eq. (6).

Due to the two-point probability function doesn't take account of the spatial continuity between two locations, such reconstruction algorithms give poor representation in terms of connectivity [14,43]. Therefore, one- and two-point probability functions are insufficient to reproduce more complex porous structures. Then, more morphological descriptors that contain connectivity information are proposed to import into reconstruction process, such as two-point cluster function, lineal-path length and chord-length function. Because it is difficult to incorporate these new descriptors into the aforementioned methods, simulated annealing method was proposed to reconstruct images subject to various statistical constrains.

#### Simulated annealing reconstruction (SAR)

Simulated annealing (SA) is a classical optimization algorithm which is developed for approximating the global optimum of the given function. As mentioned before, the greatest advantage of SA method is that it can embrace all interested descriptors in reconstruction process. Flexibility, in terms of arbitrary combination of various descriptors makes SA algorithm one of the most popular reconstruction methods currently being used. The basic idea of SA algorithm can be summarized as perturbing and annealing the initial structure to structure with the pre-set correlation functions. This procedure contains five critical operations, definition of objective function, pixel (voxel) swapping strategy, cooling mechanism, energy minimization method and termination norm [44].

##### I. Objective function

The objective function  $E_t$  is always defined as the sum of squared deviations between an arbitrary number of correlation functions obtained from reference image or experimental data and correlation functions extracted from reconstructed structure. Generally speaking,  $E_t$  is a function depends on four variables: direction  $d$ , phase  $m$ , correlation function  $q$  and length scale  $r_k$  which can be expressed as:

$$E_t = \sum_{d=1}^D \sum_{m=1}^M \sum_{q=1}^Q \sum_{r_k}^{r_{\max}} \alpha_{d,m,q} [f_0^{(d,m,q)}(r_k) - f_{r,t}^{(d,m,q)}(r_k)]^2 \quad (13)$$

Where  $f_0^{(d,m,q)}(r_k)$  presents the  $q^{\text{th}}$  correlation function of reference structure for phase  $m$  evaluated at length scale,  $r_k$ , while  $f_{r,t}^{(d,m,q)}(r_k)$  means the  $q^{\text{th}}$  correlation function of reconstructed structure for phase  $m$  evaluated at length scale,  $r_k$  in  $t^{\text{th}}$  time step.  $D$ ,  $M$  and  $Q$  denote the maximum index of direction, phase and the selected correlation function respectively. For example, if we consider four directions in 2D plane, two principle directions and two diagonal directions which are labelled as a vector [1–4], the value of  $D$  is 4 and  $d$  belongs to [1–4]. The  $r_{\max}$  is the maximum length, a correlation function over which it has influence. This influence range is similar to the length range of variogram function.

##### II. Pixel (voxel) swapping strategy

The SA algorithm is used to optimise objective function by perturbing the structure to minimize the energy,  $E_t$ . This optimisation process is performed by swapping pixels (voxels) with different phases. Pixel (voxel) swapping strategy has significant effect on the convergence speed of SA. The most original swapping strategy is random swapping, which is randomly selected two pixels (voxels) in different phases and then exchange their positions. This method has a very slow convergence due to unplanned swapping, which may destroy previously formed clusters. In order to address this issue

some researchers suggested to constrain selected pixels (voxels) by certain conditions[44]. Then, the interfacial pixel (voxel) swapping was introduced by Torquato [45], in which pixels (voxels) located at interfaces are selected for swapping.

### III. Cooling mechanism

The temperature decreasing strategy has a significant impact on the quality and speed of simulation process. A Faster reduction in temperature (cooling) might result in the process to be trapped in a local minima and a slowly reduction of temperature might lead to longer time for convergence. In order to get a balance between the need for simulation time and reaching global minima, several cooling mechanisms are introduced:

Logarithmic model [46]

$$T_k = \frac{T_0}{\log(1 + k)} \quad (14)$$

Power law model [47]

$$T_k = \lambda T_{k-1} = \lambda^k T_0 \quad (15)$$

where  $\lambda$  is the temperature reduction parameter.

### IV. Energy minimization method

Energy minimization method decides on whether to accept or reject a pixel swap which is critical for accuracy and speed of simulation process. The most straightforward strategy is to accept all energy decreasing moves and reject all energy increasing moves [48]. This algorithm is easy to implement but has high risk of being trapped in local minima when processing complex structures. The most common algorithm used for energy minimization is probability based acceptance criteria proposed by N. Metropolis [49]. The acceptance probability,  $p(\Delta E_t)$  is given as:

$$p(\Delta E_t) = \begin{cases} 1, & \Delta E_t \leq 0 \\ \exp(-\Delta E_t/T_t), & \Delta E_t > 0 \end{cases} \quad (16)$$

where  $\Delta E_t$  is the energy change due to the swap of pixels, and  $T_t$  is annealing temperature. In contrast to the Great Deluge algorithm, an increase in energy is accepted as per  $\exp(-\Delta E_t/T_t)$  to avoid the optimization process to be trapped into a local minima. In energy minimisation method, with decrease in  $T_t$  gradually results in lower probability of acceptance for energy increasing cases. As the optimisation process continues the simulation converges to the current minima (local/global).

Different from the probability based acceptance criteria, the threshold energy based energy minimization algorithm is proposed by Dueck and Scheuer [50] which is given by:

$$p(\Delta E_t) = \begin{cases} 1, & \Delta E_t \leq E_t \\ 0, & \text{otherwise} \end{cases} \quad (17)$$

where  $\Delta E_t$  is the energy change due to the swap of pixels,  $E_t$  is a positive preset threshold energy. This method constrains the chances of acceptance of moves from one configuration over other. These moves cause high energy increase. The modelling procedure starts with high threshold energy to allow all possible moves that can result in a reconstruction. During the simulation  $E_t$  is slowly reduced to decrease the acceptance probability of energy increasing swaps.

### V. Termination norm

The most common termination condition is set a tolerance between the energy of reconstructed structure and reference image. Once the objective function reaches this tolerance, simulation procedure quits. However, SA method can't guarantee the simulation converges to global minima, so the maximum failed swap number is set to stop the process. The simulation is terminated after a certain number of consecutive moves [51].

Simulated annealing method allows to arbitrary combine structure descriptors as constrains in reconstruction process, which means, it can reproduce a structure satisfying any expected statistical features in theory, but it is impractical because the reconstruction process may be trapped into a local minima and difficult to get out of the trap. In addition, its tedious computation limits building a porous structure with limited size.

### 2.3. Multiple-point reconstruction

Multiple-point reconstruction is based on the theory of Markov random field. The application of Markov Random Field (MRF) and its one-dimensional version, Markov Chain Monte Carlo (MCMC) method [33] for pore structure reconstruction is inspired by its applications in image processing, such as image-restoration and image denoising [52]. The basic idea of MRF theory is using a small number of local conditions to predict global features based on given images (training image). Generally speaking, image is pixelated, and the probability of each pixel being in a particular state (solid or void) is



				$i-2, j-1$	$i-2, j$	$i-2, j+1$	
$i-1, j-1$	$i-1, j$	$i-1, j+1$	$i-1, j-2$	$i-1, j-1$	$i-1, j$	$i-1, j+1$	$i-1, j+2$
$i, j-1$	$i, j$	$i, j+1$	$i, j-2$	$i, j-1$	$i, j$	$i, j+1$	$i, j+2$

(a) Form of neighbourhood of pixel( $i, j$ ) for the first-order case

(b) Form of neighbourhood of pixel( $i, j$ ) for the second-order case

Fig. 1. Form of neighbourhood of pixels ( $i, j$ ) for the first- and second-order case [53].

determined (or conditioned) by means of a transition matrix of conditional probabilities that is extracted from the training image [33].

The cumulative multivariable distribution function of a porous structure is defined as:  $P(\mathbf{f}) = P\{z(\vec{\mathbf{r}}_1) = z_1, z(\vec{\mathbf{r}}_2) = z_2, \dots, z(\vec{\mathbf{r}}_n) = z_n\}$ . Note that in practical term,  $P(\mathbf{f}) = P\{z(\vec{\mathbf{r}}_1) = z_1, z(\vec{\mathbf{r}}_2) = z_2, \dots, z(\vec{\mathbf{r}}_n) = z_n\} \neq \prod_{i=1}^n P(z(\vec{\mathbf{r}}_i))$ . This is because,  $P(\mathbf{f}) = \prod_{i=1}^n P(z(\vec{\mathbf{r}}_i))$  means a voxel's state is totally independent with its adjacent voxels' state, which is almost impossible in nature. The *Markov random field* describes the phenomenon that a voxel has high correlation with its neighbour voxels and this correlation gradually decreases with increase in distance. Under the frame of Markov random field, the probability of a special realization  $z(\vec{\mathbf{r}}_i)$  can be described as:

$$P(z(\vec{\mathbf{r}}_i) | z(\vec{\mathbf{r}}_1), z(\vec{\mathbf{r}}_2), \dots, z(\vec{\mathbf{r}}_n)) = P(z(\vec{\mathbf{r}}_i) | z(\mathbf{N}_i)) \quad (18)$$

Where  $\mathbf{N}_i$  is the neighbourhood of  $\vec{\mathbf{r}}_i$ .

$$P(\mathbf{f}) = \prod_{i=1}^n P(z(\vec{\mathbf{r}}_i) | z(\mathbf{N}_i)) \quad (19)$$

Then the reconstruction process involves how to define the *Neighbourhood structure* and *Conditional probabilities*. The state of any given pixel is assumed to depend on the states of its neighbour pixels. The location of these neighbour pixels form a special neighbourhood structure. Conditional probability defines the probability of a pixel that has a given state under a special neighbourhood condition. All multiple-point reconstruction methods are carried out with two steps: definition of neighbourhood structure and calculation of conditional probabilities. The initial version of MPS reconstruction is named as Markov Chain Monte Carlo (MCMC).

#### Markov Chain Monte Carlo (MCMC) reconstruction

##### 1. Neighbourhood structure of MCMC

Selection of neighbourhood structure is critical for the performance of the MRF reconstruction due to two reasons: a small neighbourhood may fail to capture the heterogeneity of training image, while a large neighbourhood always involves tedious computation. Selection of proper neighbourhood structure highly depends on the porous structure itself. Generally, first- order Gibbs chain is used to describe neighbourhood structure and is expressed as:

$$N_{1st}(i, j) = \begin{bmatrix} (i-1, j-1) & (i-1, j) & (i-1, j+1) \\ (i, j-1) & (i, j) & (i, j+1) \end{bmatrix} \quad (20)$$

The second-order Gibbs chain is given by:

$$N_{2nd}(i, j) = \begin{bmatrix} N/A & (i-2, j-1) & (i-2, j) & (i-2, j+1) & N/A \\ (i-1, j-2) & (i-1, j-1) & (i-1, j) & (i-1, j+1) & (i-1, j+2) \\ (i, j-2) & (i, j-1) & (i, j) & (i, j+1) & (i, j+2) \end{bmatrix} \quad (21)$$

The frames of first- and second-order Gibbs chains are presented in Fig. 1.

In order to build 3D porous structure, Wu et al., [33] introduced a 15-neighbourhood structure (see Fig. 2) with thirteen conditional voxels and two voxels to be decided, as shown in Eq. (22).

$$N_{15}(i, j; i, j+1, k) = \begin{bmatrix} i-2, j, k-1 & i-2, j+1, k-1 & i-1, j, k-1 \\ i-1, j+1, k-1 & i, j-1, k-1 & i, j, k-1 \\ i, j+1, k-1 & i-2, j, k & i-2, j+1, k \\ i-1, j-1, k & i-1, j, k & i-1, j+1, k \\ i, j-1, k & i, j, k & i, j+1, k \end{bmatrix} \quad (22)$$

Because the boundary voxels have no 15-neighbourhood structures, some concession strategies are used to solve this problem. At the beginning of the reconstruction, the conditional probability of the first voxel is given by Monte Carlo

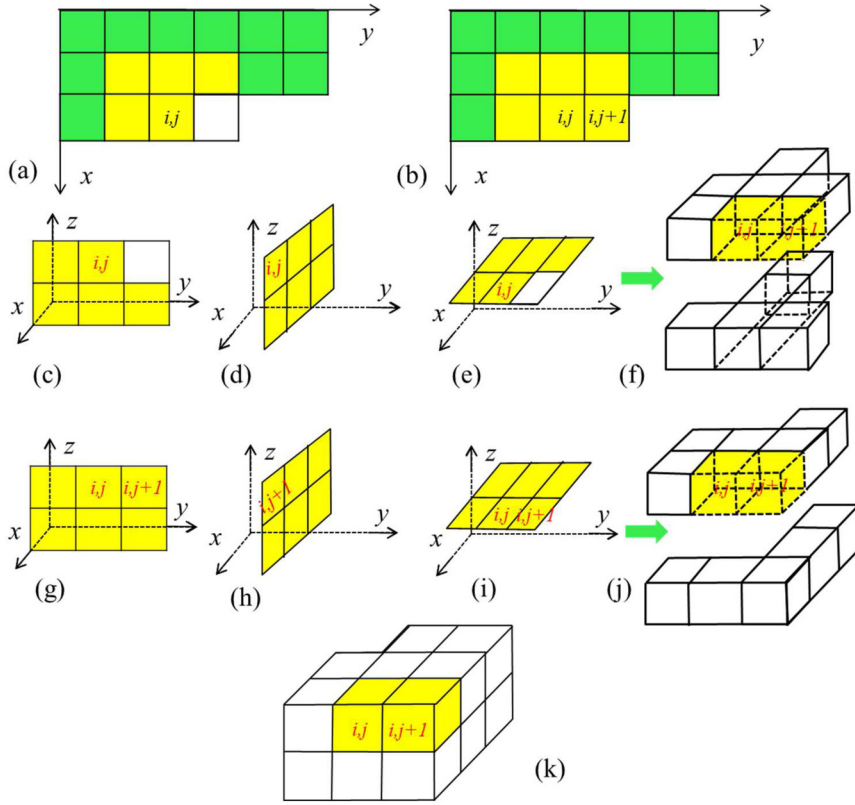


**Fig. 2.** Illustration of building 15-neighbourhoods based on combination of 2D 5- and 6-neighbourhoods structures. (a) is 2D 5-neighbourhoods structure and (b) is 2D 6-neighbourhoods structure; The neighbourhood of voxel  $(i, j, k)$  can be decomposed in to two 5-neighbourhoods structure in YZ and XY plane and a 6-neighbourhoods structure in XZ plane as shown in (c), (e) and (d) respectively; these 2D structures combine the 3D 11-neighbourhoods structure for  $(i, j, k)$ ; The neighbourhood of voxel  $(i, j+1, k)$  can be decomposed in to three 6-neighbourhoods structure in YZ, XZ and XY plane which are shown in (g), (h) and (i) respectively; these 2D structures combine the 3D 12-neighbourhoods structure for  $(i, j+1, k)$ ; (k) is the final 3D 15-neighbourhoods structure combining (f) and (j) [33].

sampling according to the porosity. Then the first row of first layer is reconstructed using a 1D 3-neighbourhoods structure. The remaining rows of the first layer start with a 4-neighbourhood structure and followed by a 5-neighbourhood structure to finish the rest voxels of the first layer.

The first row of second layer is formed similar to the second row of the first layer but using a vertical 4-neighbourhood structure. The second row of second layer starts with reduced 7- and 8-neighbourhood structure and continues with reduced 10- and 11-neighbourhood structure. Then, the inside rows and columns are built using the full 3D 15-neighbourhood structures.

As mentioned in foregoing section, the selection of neighbourhood structure needs to balance the reconstruction accuracy as well as the computational price. In general, if the computer CPU permits, a larger neighbourhood structure brings better reconstruction performance.

## II. Conditional probabilities of MCMC

One of the problems usually associated with MRFs is that all conventional Markov Chain algorithms [52] treat each pixel individually at each stage and that they are essentially iterative which is computationally intensive. Qian and Titterton [53] introduced a scanning algorithm to update the image as lines (row or column) of pixels at a time to accelerate the convergence. In order to expound the procedure of this scanning algorithm, some special notations are given as follows. For a 2D image with a size of  $M \times N$  pixels ( $M$  rows and  $N$  columns), let  $Z_i = (Z_{i1}, Z_{i2}, \dots, Z_{iN})$  denotes the  $i$ th row, where  $Z_{ij} \in \Omega$  for the state of the pixel located at  $i$ th row and  $j$ th column. Then  $Z = (Z_1, Z_2, \dots, Z_M)$  can be used to denote the whole image. Here, the first-order pairwise interaction multidimensional Markov Chain is used as an example to explain the reconstruction method. For the first row:

$$P(Z_1 = z_1) = P(z_1) = \frac{1}{C_1} \exp \left( \sum_{j=1}^N g_{1j}(z_{1j}) + \sum_{j=1}^{N-1} G_{1j}(z_{1j}, z_{1,j+1}) \right) \quad (23)$$



And, for  $i = 2, \dots, M$ ,

$$P(Z_i = z_i) = P(z_i) = \frac{1}{C_i(z_{i-1})} \exp \left( \sum_{j=1}^N \bar{g}_{ij}(z_{ij}) + \sum_{j=1}^{N-1} G_{ij}(z_{ij}, z_{i,j+1}) \right) \quad (24)$$

Where  $\bar{g}_{ij}(z_{ij})$  is given by:

$$\bar{g}_{ij}(z_{ij}) = \begin{cases} g_{ij}(z_{ij}) + G_{ij}^{(0)}(z_{i-1,j}, z_{ij}) + G_{ij}^{(1)}(z_{i-1,j+1}, z_{ij}), & j = 1 \\ g_{ij}(z_{ij}) + G_{ij}^{(-1)}(z_{i-1,j-1}, z_{ij}) + G_{ij}^{(0)}(z_{i-1,j}, z_{ij}) + G_{ij}^{(1)}(z_{i-1,j+1}, z_{ij}), & 2 \leq j \leq N-1 \\ g_{ij}(z_{ij}) + G_{ij}^{(-1)}(z_{i-1,j-1}, z_{ij}) + G_{ij}^{(0)}(z_{i-1,j}, z_{ij}), & j = N \end{cases} \quad (25)$$

In Qian and Titterton [53] model,  $g_{ij}$  and  $G_{ij}$  are given by:

$$\begin{cases} g_{ij}(z_{ij}) = 0, \forall i, j, \\ G_{ij}(z_{ij}, z_{i,j+1}) = \beta I(z_{ij}, z_{i,j+1}) \\ G_{ij}^{(-1)}(z_{i-1,j-1}, z_{ij}) = \beta_{-1} I(z_{i-1,j-1}, z_{ij}) \\ G_{ij}^{(0)}(z_{i-1,j}, z_{ij}) = \beta_0 I(z_{i-1,j}, z_{ij}) \\ G_{ij}^{(1)}(z_{i-1,j+1}, z_{ij}) = \beta_1 I(z_{i-1,j+1}, z_{ij}) \end{cases} \quad (26)$$

And the indicator function  $I(s, t)$  satisfies:

$$I(s, t) = \begin{cases} 1, & s = t \\ 0, & \text{otherwise} \end{cases} \quad (27)$$

Obviously, the advantage of this method is that the neighbourhood interactions of an entire image can be represented by relatively few parameters. The potential function can be expressed as a linear function of the parameters, so the parameters can be estimated applying maximum-likelihood methods [53]. However, this is insufficient to reproduce some complex porous structures which contain relatively long-range correlations. This is because the simplifying assumptions of the linear formulation of the potential functions are incompatible with complex image structure. In order to solve this problem, an alternative method based on direct measurement of the conditional probabilities associated with all possible configurations of the given neighbourhood structure based on training image is developed [54].

#### Multiple-point statistics reconstruction (MPS)

Multiple-point statistics (MPS) can be treated as a generalization of MRF method. The correlation functions discussed before can be treated as various kinds of conditional probabilities. In general, stricter the condition is, more determinate the information obtained. To this note, multiple-point probability function (multiple-point statistics) is introduced to extend the two-point correlation functions to multiple-point probability function for more complex structure [55–58]. MPS algorithm is developed rapidly in field scale modelling [59–63] and then introduced into 3D porous structure reconstruction at micro scale [34,64]. Using the definition of  $n$ -point correlation function discussed before, the multiple-point probability function can be defined as follows:

$$S_m^{(j)}(\vec{r}) = \langle I^{(j)}(P_{\vec{r}}) \rangle \quad (28)$$

Where  $N_{\vec{r}}$  defines a neighbourhood of centre point and  $P_{\vec{r}}$  is the data event (pattern) recorded by template:

$$P_{\vec{r}} = (v_{n_1}, v_{n_2}, v_{n_3}, \dots, v_{n_m}), (n_1, n_2, n_3, \dots, n_m \in N_{\vec{r}}) \quad (29)$$

And  $I(P_{\vec{r}})$  represents all pixels or voxels of training image whose neighbourhood matches with  $P_{\vec{r}}$ . Within these matched events, if the facies of the centre pixel or voxel is  $j$ , then the characteristic function,  $I^{(j)}(P_{\vec{r}})$  is valued as 1, otherwise is 0.

$$I^{(j)}(P_{\vec{r}}) = \begin{cases} 1, & \text{where } \vec{r} \text{ is in phase } j \\ 0, & \text{otherwise} \end{cases} \quad (30)$$

Multiple-point probability function can be defined as the probability of a given pixel whose phase is  $j$  under a special neighbourhood condition (see Fig. 3).

Basic procedure of multiple-point statistic algorithm can be summarized in three steps:

Firstly, a random path is set to visit all un-estimated voxels in the reconstruction domain and then the subsequent reconstruction work is carried out along this path.

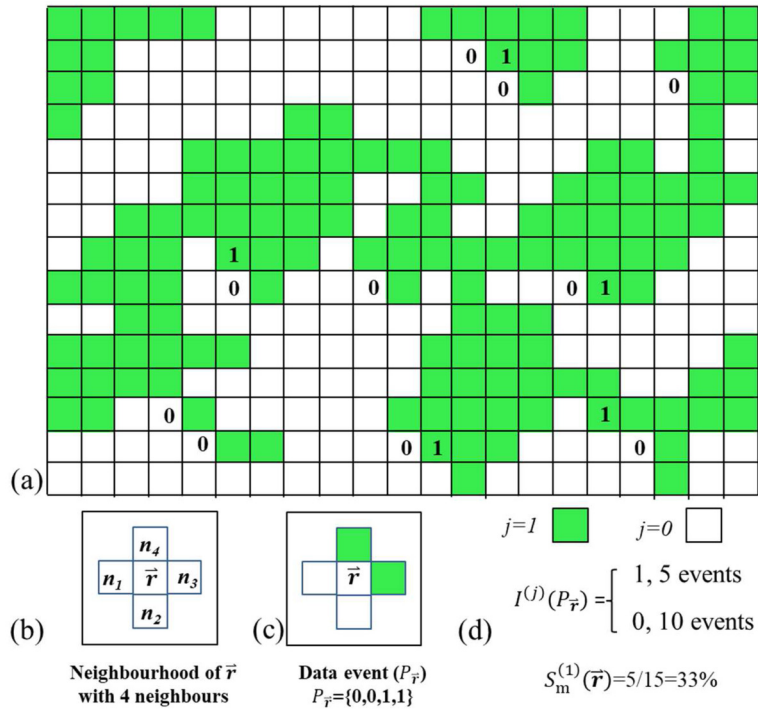


**Fig. 3.** An illustration of Multiple-point phases pattern extraction. (a) is a  $15 \times 21$  pixels training image with two phases of pore (green) and solid (white), where pore and solid are denoted by 1 and 0, respectively. (b) defines a unique structure with 4 neighbourhood. (c) presents a special pattern of the structure (b); and (d) is the statistical results of the pattern (c) based on the training image (a). It shows that 15 matched patterns are totally found in the training image (a), where 5 events' centre pixel's phase is 1 and 10 events' centre pixel's phase is 0, therefore the obtained probability of the centre pixel's phase is 1, ( $S_m^{(1)}(\vec{r})$ ) of the given pattern is 33%. (For interpretation of the colours in the figure(s), the reader is referred to the web version of this article.)

Secondly, for any specific voxel, the search tree is retrieved to find out the conditional probabilities corresponding to the data event of this voxel. The retrieve work starts from a large template size. If the corresponding data event is not searched in the search tree, a decreased size template is used to repeat until the proper conditional probabilities are obtained.

Thirdly, a specific phase (e.g., solid or void) is selected for the current voxel using Monte Carlo sampling based on the conditional probabilities obtained in the second step.

Implementation of MPS reconstruction has two major road-blocks which halted its application for years. Firstly, because of the limited size of training image practically available and therefore, there are not enough replicas available for each data event. Secondly, because of the repeated scanning of training image for simulation of every voxel, it is always time-consuming to reconstruct a relatively large porous medium.

### I. Multi-Grid Simulation

In theory, larger the template is, better is the reproduction of the geometric features of the training image. In practice, however, the template size is limited by the CPU and RAM costs and also by the size of training image. If, the template size is too small it fails to capture long-range patterns of the training image.

In order to balance the template size and computation time, a multiple-scale template strategy is applied. In this method, relatively larger template is applied to scan the training image, if there is no sufficient number of replicas are obtained, a set of templates with progressively reduced size is used until a designated minimum number of replicas of  $P_{\vec{r}}$  are searched [34]. When used large size templet, not enough replicas can be found due to the limitation of training image size. One effective approach to capture the large scale structure with manageable data size for every data event is to use multi-grid strategy proposed by Hernandez [65] and later extended by Tran [66] in 1994. In multiple-grid simulation, the simulation work is firstly carried out on a coarse grid. Then in each of the subsequent steps, simulation is performed on a finer grid until the finest grid is completed [67]. In each grid level simulation, patterns are also extracted at corresponding grid level from training image (see Fig. 4). When the visit path is selected properly, parallel computing can be employed to accelerate the computation significantly.

### II. Search Tree

Initial implementation of MPS reconstruction needs to scan the training image every time for each point's estimation, which is extremely time-consuming. To avoid scanning the training image repeatedly, Strebelle [68] introduced a new data structure called search tree for storing the multiple-point statistics extracted from training image. In order to describe the

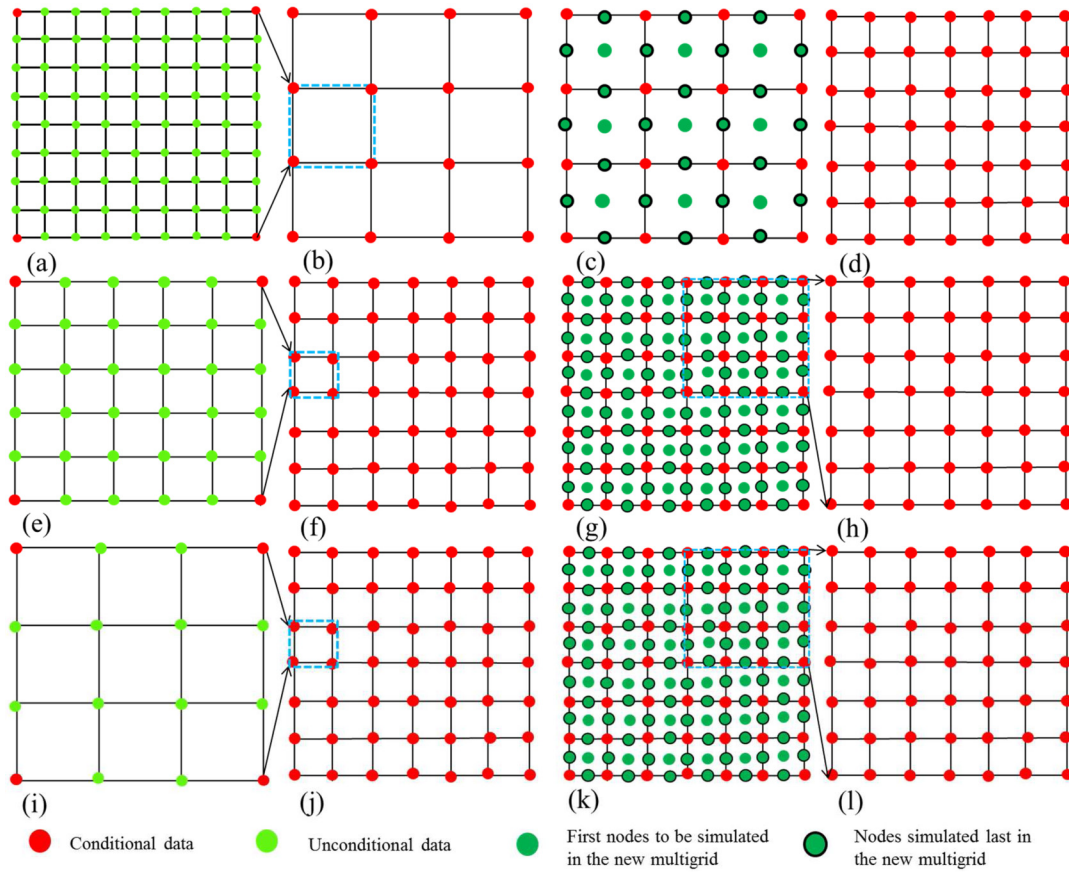


**Fig. 4.** (a): A schematic of multigrid simulation procedure with a three scales strategy. (b) A  $4 \times 4$  coarse grid system with 16 conditional data and each lattice contains a  $9 \times 9$  subscale grid system shown in (a). Fig. 5 (c) the coarse grid level estimation, in which the central nodes of each coarse grid are estimated first and then the boundary central nodes. (d) The result of coarse grid level estimation. (f) The initial status of intermediate grid level estimation which is identical with (d). Every lattice within (f) is a  $5 \times 5$  subscale grid system shown in (e). (g) Intermediate estimation procedure. For convenience, the result of intermediate estimation is shown in quarter part in (h). (j) Initial status of finest grid level estimation and each lattice contains a  $4 \times 4$  grid system as shown in (i). (k) Is the finest grid level estimation and part of its result is shown in (l).

building of a search tree,  $r_1, r_2, \dots, r_m$  are used to denote a data template with a central point being  $r_0$ . These points are ordered according to their distance from the central point,  $r_0$  from nearest to farthest. Then a set of nodes are linked to establish a tree structure, each node records a specific data event. The search tree has  $m + 1$  layers from root layer (layer 0) to deepest layer (layer  $m$ ). The root node represents the event that there is no condition data. The number of condition data increases along with the growing of layers. At each node, the search tree splits up to  $k$  branches, where  $k$  denotes the number of facies. From second layer, every node records a data event with one more neighbour compared with its former layer. Nodes corresponding to data events, for which at least one replica is found in the training image, are presented in the search tree (see Fig. 5).

Fig. 5 demonstrates the procedure of building of a search tree. Fig. 5(a) is a  $4 \times 4$  pixels training image in which green colour denotes 0 and white colour denotes 1. Fig. 5(b) defines a 4-neighbour data template denoted by  $(r_1, r_2, r_3, r_4)$ . Fig. 5(c) is the search tree extracted from (a) and (b). The number at lower left corner of  $r_0$  records the number of replicas of green facies while the upper right corner records the number of replicas of white facies.

The MPS method was first introduced by Okabe and Blunt to build a realistic 3D porous structure with manageable computing resources when only 2D thin section image is available [34]. They reconstructed a 3D pore space structure by assuming isotropy in orthogonal directions and building a pseudo-3D training image from the data events extracted from the 2D image. Alireza, et al., [70] proposed a MPS reconstruction strategy where the reconstruction is carried out layer by layer in a 2D plane instead of building a 3D pseudo-training image. Within every layer, the Single Normal Equation Simulation (SNESIM) [71] is used to realize the 2D reconstruction. The continuity between two adjacent layers is guaranteed by multi-scale conditional data extracted from former reconstructed adjacent layer. Compared to Truncated Gaussian Simulation Model Reconstruction (TGSIMR) and Sequential Indicator Simulation Model Reconstruction (SISIMR), MPS method uses multiple-point statistics as descriptor rather than two-point probability functions which means it is more effective to reproduce the intrinsic properties of the porous media. MPS method has been successfully used to reconstruct the inner structure of sandstone [72,73] and carbonate rock [34,35].

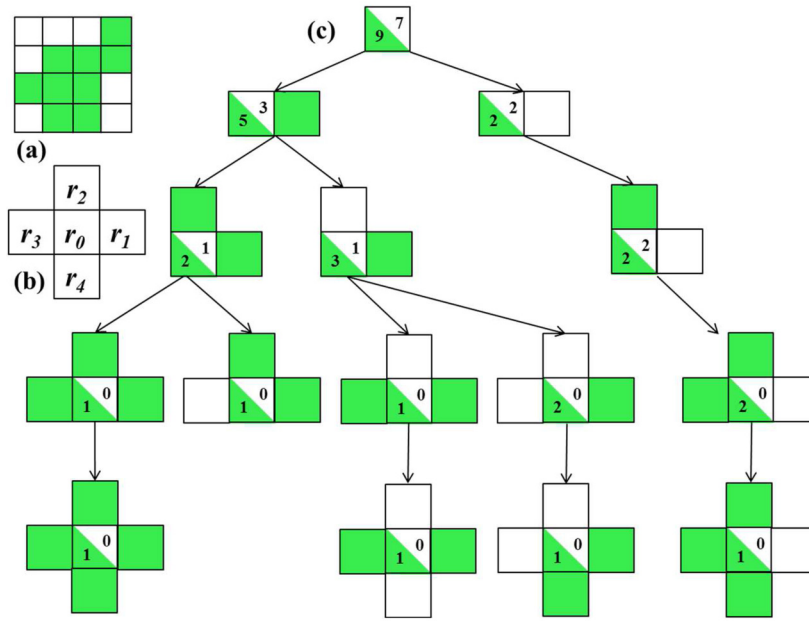


**Fig. 5.** (a) A training image; (b) a 4-neighbours data template; (c) a constructed search tree from (a), adapted by [69].

#### Pattern-based MPS reconstruction

As discussed in previous section, voxel-based reconstruction leads to tedious computation. In order to solve this problem, pattern-based MPS reconstruction was proposed. In this pattern based MPS approach reconstruction of a porous structure is carried out pattern by pattern. In fact, pattern-based MPS can be treated as an object-based reconstruction method. Pattern-Based MPS reconstruction is carried out via two steps: pattern classification and pattern simulation.

Firstly, a template,  $T$  is used to scan the whole training image to extract all existing patterns of the training image. Identical patterns are collected together as a pattern class and the frequency of each pattern class can be calculated. Then simulation process is carried out based on the sequential paradigm. A non-estimated point ( $\vec{r}$ ) is selected from the simulation field, and its conditioning data event (denoted by  $dev_T(\vec{r})$ ) in its neighbourhood is identified. The most compatible pattern selected from the pattern database is patched onto the simulation field. During the reconstruction, it is possible that more than one pattern are compatible with the event data in which case one of these patterns is selected randomly based on their frequency. Using a raster path to visit the simulation field, the above algorithm is undertaken repeatedly until the whole porous structure is reconstructed [74–76].

The greatest challenge of this pattern-based reconstruction method is how to deal with the potential discontinuities between two simulated patches. One solution is to set an overlap area between two blocks and the points with overlap area is applied as condition data for following blocks reconstruction. However, a problem may raise when the template  $T$  is very large or when the training image is not informative enough to support the condition data. This can lead to a situation that there is no matched pattern can be found in pattern database. In this case, the target block is split into smaller data events until the pattern, that matches the condition data, can be found in training image. Fig. 6 illustrates the adaptive recursive template splitting for pattern-based reconstruction using an imaginary example with 4 patches simulation field. Fig. 6(a) presents the initial status of reconstruction where the first patch with a data event of  $dev_T(\vec{r}_1)$  has been reconstructed and the second one ( $dev_T(\vec{r}_2)$ ) is the next candidate for estimation. The green area is overlap part between first and second patch which is used as condition data for the reconstruction of second patch. Assuming that a matched pattern is successfully searched from data event database for the second patch, and then the reconstruction steps into the third patch with a data event,  $dev_T(\vec{r}_3)$  (see Fig. 6(b)). Fig. 6(c) illustrates a situation that there is no matched pattern for whole third patch, then the target patch is divided into smaller patches denoted by  $dev_T^{s1}(\vec{r}_3)$ . Fig. 6(d) and (e) show that the sub-patches,  $dev_T^{s2}(\vec{r}_3)$  and  $dev_T^{s3}(\vec{r}_3)$  which are successfully reconstructed. However, the sub-patch,  $dev_T^{s3}(\vec{r}_3)$  has no match patterns in data event database. In this situation, the sub-patch,  $dev_T^{s3}(\vec{r}_3)$  is further divided into smaller patches for reconstruction (see Fig. 6(f)). This process is recursively carried out until the whole simulation field is established.

Pattern-based MPS method is not only suitable for simulating categorical variables [77], also capable for continuous simulation [74,78]. In order to carry out continuously variable reconstruction, there are in general few replicas of particular local pattern even when a large training image is available [69]. One solution to this situation is to discretise the continuous variables into a certain number of categories and then use the categorical variable reconstruction. Another solution is to define a distance to calculate the similarity (instead of identical) between target data event with patterns in data event database. For example, Tahmasebi, Hezarkhani and Sahimi [74] proposed to use cross-correlation function to quantify the similarity between target data event with patterns in data event database. Zhang [79] proposed a filter-based simulation

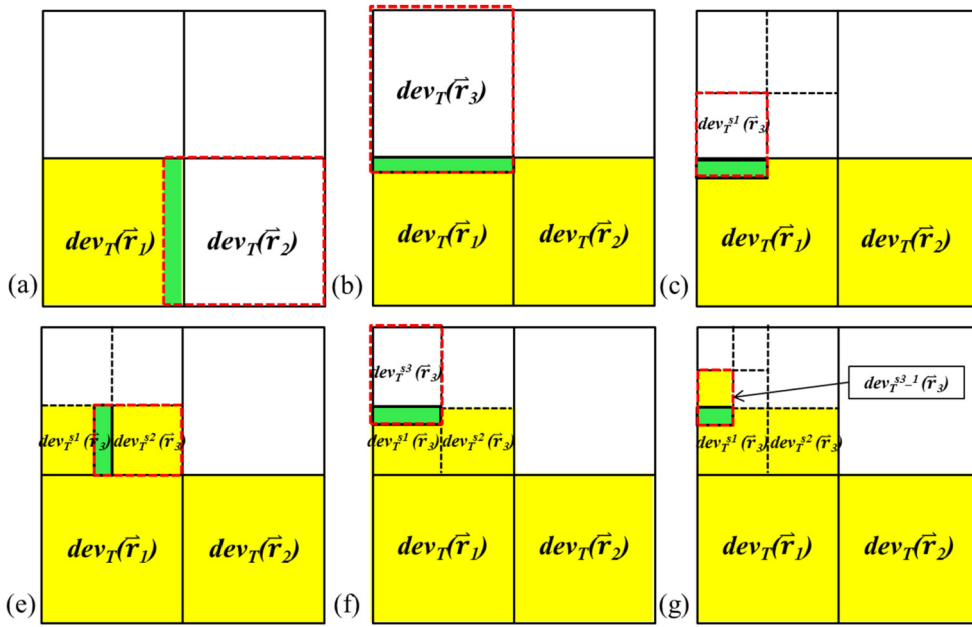


**Fig. 6.** Adaptive recursive template splitting for pattern-based MPS reconstruction. From (a) to (g), an imaginary reconstruction process is illustrated. (c) and (g) show the situation that there is no matched patterns that can be found in the data event database and then a splitting strategy is used to continue the reconstruction. Yellow areas denote the reconstructed patch, green areas denote the overlap area and white areas denote the candidate patches which are waiting for estimation. The red box presents the current estimation patch. (Adapted by [74]).

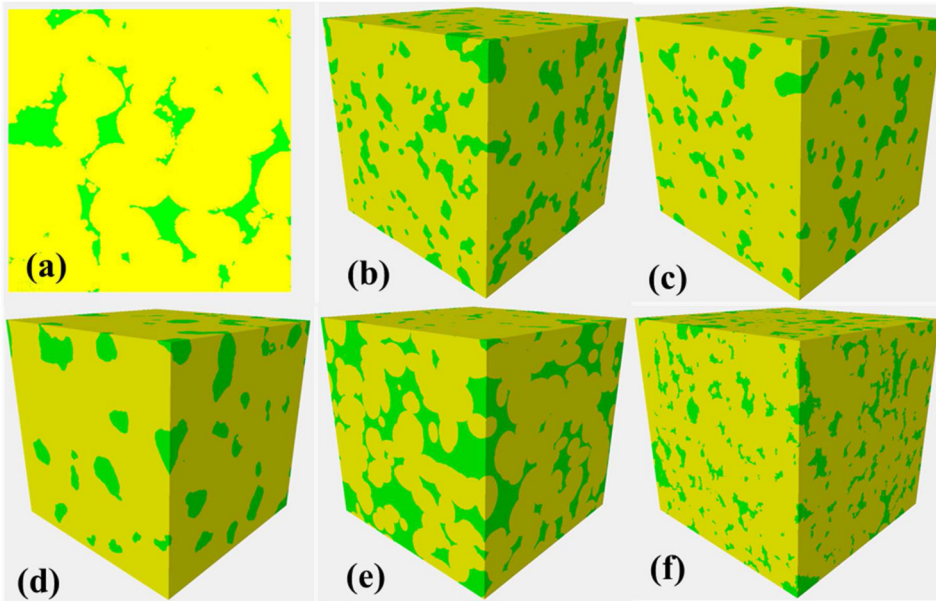


**Fig. 7.** An illustration of the pore structures reconstructed by different methods, (a) is 2D training image, (b) is Kriging interpolation result, (c) is Gaussian Random Field reconstructed image, (d) is Simulated Annealing reconstructed image, (e) is the result of the process-based reconstruction, and (f) is multiple point statistic method reconstructed image.

(FILTERSIM) method to significantly reduce the dimensionality of training patterns and consequent RAM demand. In this method, the training images are scanned by a set of filters. Then the local training patterns and textures are classified by the set of filter scores which can be used as similarity retrieve item in subsequent reconstruction.

Fig. 7 illustrates the reconstruction results of different methods including Kriging interpolation, Gaussian random field, simulated annealing, process-based reconstruction, and multiple point statistics. Note that the images presented in Fig. 7 just qualitatively compare the structure features reconstructed by different methods. The reconstruction performance of a given method significantly influenced by the selection of various modelling parameters.



## 2.4. Multiple-resolution training images reconstruction

Multiple-resolution training images is carried out to build a 3D high resolution porous structure based on low resolution  $\mu$ -CT image and high resolution 2D section(s) [80]. Because the application of  $\mu$ -CT images, it is not difficult to obtain the 3D porous structure of rock sample directly. The point is how to improve the resolution of the porous structure obtained from  $\mu$ -CT image(s) rather than reconstruct a 3D porous structure from 2D section(s). The porous structure using  $\mu$ -CT image(s) as hard data has a significant advantage that the  $\mu$ -CT image contains information on the heterogeneity of the target sample.

### Hybrid superimpose reconstruction

Along with the universally use of  $\mu$ -CT, a hybrid strategy is proposed to generate more deterministic 3D image in which the low frequency information is obtained from  $\mu$ -CT image directly and then supplement high frequency content extracted from high resolution 2D images. Okabe and Blunt [81] introduced a method to recover the small features lost in low resolution  $\mu$ -CT image by combining 2D SEM images with 3D low resolution  $\mu$ -CT image. In this approach macro-pores are identified by  $\mu$ -CT while micro-pores are generated by MPS reconstruction method based on SEM image. Then the two images are superimposed to obtain the final image with an improved image quality. This hybrid strategy is extended to a multiresolution and multiscale modelling to address the problems associated with computational cost and multiscale features reproduction [82–84]. In this method, low resolution image is applied to reconstruct the large-scale features in shale sample and high resolution 2D images are used to reconstruct the nanoscale structural features. Then, the multiscale pore network is obtained by overlying the micro and macro 3D models. In some cases, the macro scale reconstruction can be skipped if a 3D macro image is directly available.

### Neural networks reconstruction

Mosser et al., [85] proposed a 3D porous structure reconstruction method using generative adversarial neural networks. In this method, a 3D segmented training image is split into a large number of image cubes. These image cubes are ‘real’ images which are labelled as 1. Then a GAN model consists of two differentiable functions, a discriminator D and a generator G, is established. The generator G is used to transfer a randomly generated vector to a synthetic realization. The discriminator’s role is to determine whether an image cube is from training cube dataset or from the generator. The misclassification error is computed by binary cross-entropy and then back-propagated to improve the produced samples and ‘fool’ the discriminator. The aim of this process is to obtain a generator who can build a synthetic sample that the discriminator cannot identify if it is ‘real’ or ‘artificial’. Finally, the obtained generator can be used to build a large porous structure of the target sample [36].

Currently, it is not difficult to get an inch cubed  $\mu$ -CT image of the rock sample. However, the resolution of the  $\mu$ -CT image is always insufficient to capture the small structures of the sample. In order to overcome the image resolution issue Wang et al., [37] proposed a reconstruction method using convolutional neural networks to build a high resolution porous structure based on low resolution  $\mu$ -CT image. The proposed method is undertaken through following steps. Firstly, a three-dimensional low-resolution tomographic image of a rock sample is obtained by  $\mu$ -CT scanning. Then, one or more sections in the rock sample are selected to be scanned by SEM to obtain high-resolution two-dimensional images (step 1 in Fig. 8). Secondly, the high-resolution SEM image is segmented (step 2 in Fig. 8). Thirdly, the low resolution  $\mu$ -CT image is interpolated to have the same voxel size with that of SEM image (step 3 in Fig. 8). Fourthly, the section which corresponds to the high-resolution SEM image is searched from  $\mu$ -CT image by image registration. Then a large number of image patches are extracted from  $\mu$ -CT section and every image patch is labelled by the phase type of its central pixel. This phase type is given by high resolution segmented SEM image (step 4 and step 5 in Fig. 8). Afterward, the high-resolution segmented SEM images and their corresponding low-resolution  $\mu$ -CT slices are applied to train a convolutional neural network (CNN) model (step 6 in Fig. 8). Finally, the trained CNN model is used to reconstruct the entire low-resolution three-dimensional  $\mu$ -CT image (step 7 in Fig. 8). Because the SEM images are segmented and have a higher resolution than the  $\mu$ -CT image, this algorithm integrates the super resolution and segmentation processes. The input data are low-resolution tomographic  $\mu$ -CT images, and the output data are high-resolution segmented porous structures.

Convolutional neural networks can be dated back to 1989 [86] but have been neglected for a long time until recent years mainly because of two factors: (1) the efficient training implementation on modern powerful GPUs [87], and (2) the easy access to an abundance of data for training large models [88]. Similar to the conventional neural network model, a CNN model also has one input layer and one output layer, as well as a number of hidden layers. In a typical CNN model, there are three main types of layers: convolutional layer, pooling layer and fully connected layer [89]. In some cases, a flatten layer is needed between the fully connected layer and convolutional layer or pooling layer to reshape the two-dimensional or three-dimensional neural nodes to be one-dimensional. Recently, a scheme using convolution with a stride of 2 instead of pooling has been proposed to improve the training stability [90,91]. All of the layers in a CNN model will be stacked to establish the convolutional neural network architecture. In general, most of the deep learning use a feedforward neural network architecture, which learns to map a fixed-size input (e.g., an image) to a fixed-size output (e.g., a probability for each of several categories). To move from one layer to the next, a set of units computes a weighted sum of their inputs from the previous layer and passes the result through a non-linear function [92].



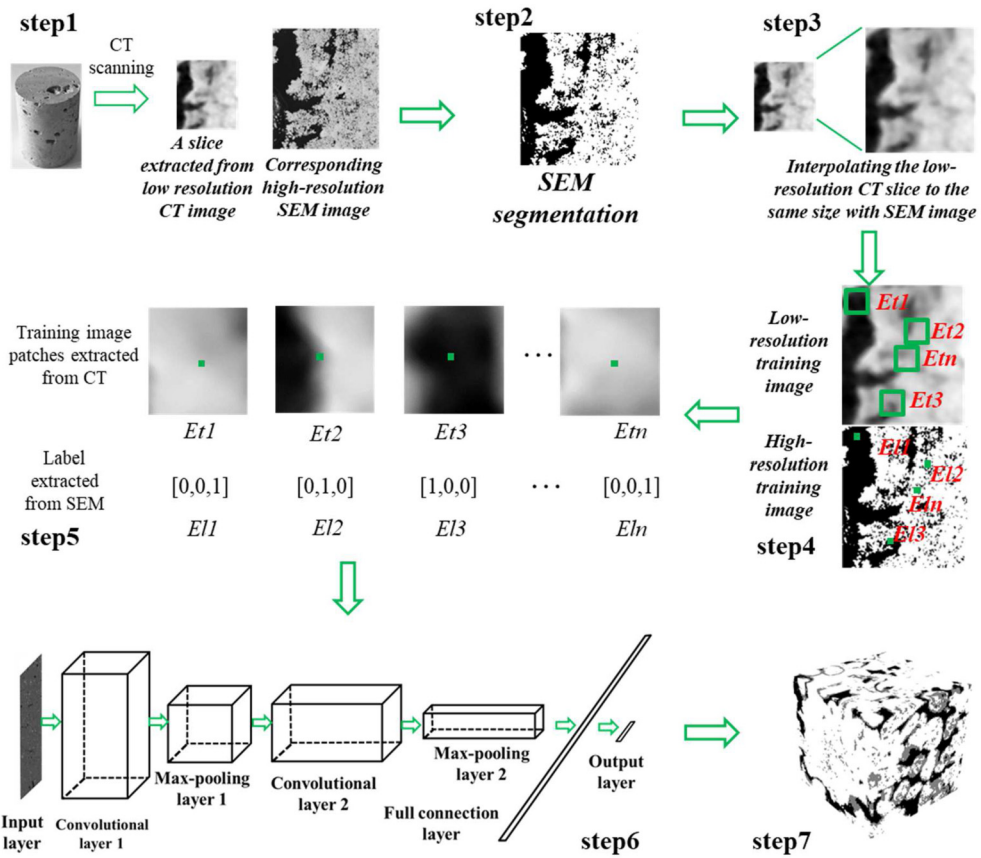


**Fig. 8.** A typical procedure of the pore structure reconstruction based on  $\mu$ -CT and SEM images using convolutional neural networks.

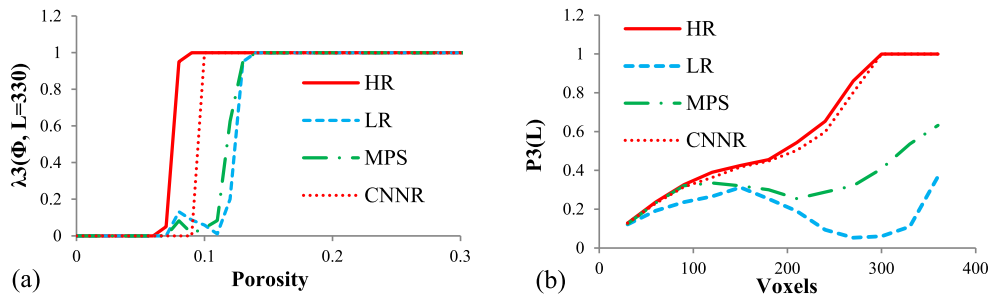


**Fig. 9.** The reconstruction performance of different reconstruction methods using Local porosity theory, where HR, LR, MPS, and CNNR stand for high-resolution reference image, low-resolution reference image, MPS reconstructed image, and CNNR reconstructed image, respectively. (a) is the local percolation probabilities distribution and (b) is the total fraction of the percolation cells curve. To a reconstructed image, the closer LPT curve to that of HR image means the better reconstruction performance.

Fig. 9 compares the performance of MPS and CNNR using local porosity theory parameters as measurement. A rock sample is scanned by  $\mu$ -CT with low resolution and four-time higher resolution respectively. The top layer of high-resolution image is applied as high-resolution training image. Note that this high-resolution training image is a 2D section. Then two high resolution reconstructed images are generated by MPS and CNNR method respectively based on low resolution  $\mu$ -CT image and high-resolution training image. The scanned high resolution  $\mu$ -CT image is then used as reference image to estimate the performance of MPS and CNNR methods. It can be seen from local percolation probabilities distribution (see Fig. 9(a)) and total fraction of the percolation cells curve (see Fig. 9(b)), the performance of CNNR method is significantly better than that of Local Similarity Super Resolution reconstruction (LSSRR) and MPS.

### 3. Conclusion

3D Pore scale numerical modelling of reservoir is very challenging, because the existing imaging techniques have inherent limitations, in terms of resolution and field of view. In this paper, we reviewed the pore scale numerical modelling methods from kriging interpolation to local-similarity statistical reconstruction.

Gaussian random field reconstruction is a means for generating multiple equiprobable realizations of the petrophysical properties in question. Essentially, some noise is added artificially into the simulation to undo the smoothing effect of kriging interpolation. This possibly gives a better representation of natural variability of the properties in question and gives us a means for quantifying the uncertainty of these properties of naturally occurring porous media. However, GRF methods need a premise that the reconstructed field is limited as Gaussian random field. This limitation can be solved by sequential indicator simulation method which is very similar to GRF methods but without the Gaussian random field assumption. Gaussian random field and sequential indicator simulation use two-point correlation functions (e.g., covariance or variogram) as priori to supervise the following reconstruction. These two-point correlation functions contain no connectivity information about pore space as a result of which the reconstructed porous structure lacks expected long range connectivity.

Simulated annealing allows importing arbitrary descriptors into the process of reconstruction as constraints. In theory, SA method can reproduce any expected structural features as long as their corresponding descriptors are imported into the objective function. This is, however, not practical due to two reasons. Firstly, the simulation may be trapped in to a local-rather than global-minimum. Secondly, although some effective strategies have been introduced to accelerate the modelling process, generating large 3D porous structure remains a heavy burden on CPU and RAM of computers.

Introduction of Markov random field facilitated for the first time to extend use of two-point statistics to multiple-point statistics in reconstruction of porous structure. In addition, MRF reconstruction is based on the multivariate statistics directly inferred from training images instead of an explicit random function model. Multiple-point statistic method is a generalization of MRF reconstruction by redefining the neighbourhood and measure the conditional probabilities associated with all possible configurations of the given neighbourhood structure directly from training image. In theory, MPS method can reproduce any expected structural features. However, the limitation of size of training image and template make it impractical in real situation. In one hand, enough size of template is the premise of reproduction of long-range connectivity. On the other, larger template results in more difficult to obtain sufficient number of replicates. Although the application of multigrid strategy relieves this struggle, it is still far from perfect to reproduce the complex porous structure, especially for heterogeneous and multiphase samples.

Process-based reconstruction (object-based reconstruction) offers an alternate approach for porous structure modelling and has some successful precedents in sandstone and chalk. However, understanding of physical and chemical processes pertaining to formation of the porous structure is essential for use of this method, which is always difficult, especially in carbonates and shales.

Development of hybrid strategy, which combines hard data acquired by imaging and numerical modelling (Convolutional Neural Network), has allowed for the first time to generate more deterministic 3D image. In this approach the low frequency data acquired by  $\mu$ -CT imaging and then supplement with high frequency content extracted from 2D images (SEM). The application of neural network model greatly improves the connectivity of pores and has a better performance than that of conventional methods including MPS.

### CRedit authorship contribution statement

**Yuzhu Wang:** Designed this study, collected data, reviewed literatures and completed the manuscript. **Sheik S. Rahman:** reviewed the manuscript.

### Declaration of competing interest

The authors declare that they have no known competing financial interests or personal relationships that could have appeared to influence the work reported in this paper.

### Data availability

No data was used for the research described in the article.

### References

- [1] N.A. Solano, C.R. Clarkson, F. Krause, R. Lenormand, J.E. Barclay, R. Aguilera, Drill cuttings and characterization of tight gas reservoirs - an example from the Nikanassin Fm. in the Deep Basin of Alberta, in: SPE Canadian Unconventional Resources Conference, Calgary, Alberta, Canada, 2012.
- [2] J. Sliwinski, M.L. Strat, M. Dublonko, A new quantitative method for analysis of drill cuttings and core for geologic, diagenetic and reservoir evaluation, in: 2009 CSPG CSEG CWLS Convention, Calgary, Alberta, Canada, 2009.
- [3] R. Rahmani, R.E. Ferrell, J.R. Smith, Multiscale Imaging of Fixed-Cutter-Drill-Bit-Generated Shale Cuttings, 2016.
- [4] G. Chalmers, R.M. Bustin, I.M. Power, Characterization of gas shale pore systems by porosimetry, pycnometry, surface area, and field emission scanning electron microscopy/transmission electron microscopy image analyses: examples from the Barnett, Woodford, Haynesville, Marcellus, and Doig units, *Am. Assoc. Pet. Geol. Bull.* 96 (6) (2012) 20.

- [5] T. Dong, N.B. Harris, Pore size distribution and morphology in the Horn River shale, middle and upper Devonian, northeastern British Columbia, Canada, *Am. Assoc. Pet. Geol. Bull.* 102 (2013) 67–79.
- [6] A. Fogden, S. Latham, T. McKay, R. Marathe, M. Turner, A. Kingston, T. Senden, Micro-CT analysis of pores and organics in unconventional using novel contrast strategies, in: *Unconventional Resources Technology Conference*, Unconventional Resources Technology Conference, Denver, Colorado, USA, 2014.
- [7] L. Chen, L. Zhang, Q. Kang, H.S. Viswanathan, J. Yao, W. Tao, Nanoscale simulation of shale transport properties using the lattice Boltzmann method: permeability and diffusivity, *Sci. Rep.* 5 (2015) 8089.
- [8] J.H. Dunsmuir, S.R. Ferguson, K.L. D'Amico, J.P. Stokes, X-ray microtomography: a new tool for the characterization of porous media, in: *SPE Annual Technical Conference and Exhibition*, Dallas, Texas, 1991.
- [9] P. Spanne, J.F. Thovert, C.J. Jacquin, W.B. Lindquist, K.W. Jones, P.M. Adler, Synchrotron computed microtomography of porous media: topology and transports, *Phys. Rev. Lett.* 73 (1994) 2001–2004.
- [10] D. Wildenschild, C.M.P. Vaz, M.L. Rivers, D. Rikard, B.S.B. Christensen, Using X-ray computed tomography in hydrology: systems, resolutions, and limitations, *J. Hydrol.* 267 (2002) 285–297.
- [11] A. Mehmani, M. Prodanović, F. Javadpour, Multiscale, multiphysics network modeling of shale matrix gas flows, *Transp. Porous Media* 99 (2013) 377–390.
- [12] J.A. Quiblier, A new three-dimensional modeling technique for studying porous media, *J. Colloid Interface Sci.* 98 (1984) 84–102.
- [13] C.L.Y. Yeong, S. Torquato, Reconstructing random media, *Phys. Rev. E* 57 (1998) 495–506.
- [14] H. Okabe, Pore-Scale Modelling of Carbonates, 2004.
- [15] P.M. Adler, C.G. Jacquin, J.A. Quiblier, Flow in simulated porous media, *Int. J. Multiph. Flow* 16 (1990) 691–712.
- [16] P.M. Adler, C.G. Jacquin, J.F. Thovert, The formation factor of reconstructed porous media, *Water Resour. Res.* 28 (1992) 1571–1576.
- [17] A.P. Roberts, Statistical reconstruction of three-dimensional porous media from two-dimensional images, *Phys. Rev. E* 56 (1997) 3203–3212.
- [18] Z.R. Liang, C.P. Fernandes, F.S. Magnani, P.C. Philippi, A reconstruction technique for three-dimensional porous media using image analysis and Fourier transforms, *J. Pet. Sci. Eng.* 21 (1998) 273–283.
- [19] A.P. Roberts, S. Torquato, Chord-distribution functions of three-dimensional random media: approximate first-passage times of Gaussian processes, *Phys. Rev. E* 59 (1999) 4953–4963.
- [20] B. Frederic, J. Dominique, Modelling a food microstructure by random sets, *Image Anal. Stereol.* 23 (2004) 33–44.
- [21] B. Biswal, R. Hilfer, Microstructure analysis of reconstructed porous media, *Phys. A, Stat. Mech. Appl.* 266 (1999) 307–311.
- [22] M.D. Rintoul, S. Torquato, Reconstruction of the structure of dispersions, *J. Colloid Interface Sci.* 186 (1997) 467–476.
- [23] C.L.Y. Yeong, S. Torquato, Reconstructing random media. II. Three-dimensional media from two-dimensional cuts, *Phys. Rev. E* 58 (1998) 224–233.
- [24] L.M. Pant, S.K. Mitra, M. Secanell, Multigrid hierarchical simulated annealing method for reconstructing heterogeneous media, *Phys. Rev. E* 92 (2015) 063303.
- [25] C. Manwart, S. Torquato, R. Hilfer, Stochastic reconstruction of sandstones, *Phys. Rev. E* 62 (2000) 893–899.
- [26] M.S. Talukdar, O. Torsaeter, M.A. Ioannidis, J.J. Howard, Stochastic reconstruction of chalk from 2D images, *Transp. Porous Media* 48 (2002) 101–123.
- [27] P. Čapek, V. Hejtmánek, L. Brabec, A. Zikánová, M. Kočířik, Stochastic reconstruction of particulate media using simulated annealing: improving pore connectivity, *Transp. Porous Media* 76 (2009) 179–198.
- [28] P.-E. Øren, S. Bakke, Process based reconstruction of sandstones and prediction of transport properties, *Transp. Porous Media* 46 (2002) 311–343.
- [29] S. Bryant, M. Blunt, Prediction of relative permeability in simple porous media, *Phys. Rev. A* 46 (1992) 2004–2011.
- [30] D. Coelho, J.F. Thovert, P.M. Adler, Geometrical and transport properties of random packings of spheres and aspherical particles, *Phys. Rev. E* 55 (1997) 1959–1978.
- [31] J.-P. Latham, Y. Lu, A. Munjiza, A random method for simulating loose packs of angular particles using tetrahedra, *Geotechnique* 51 (2001) 871–879.
- [32] F.J. Lucia, *Carbonate Reservoir Characterization*, Springer-Verlag, Berlin, 1999.
- [33] K. Wu, M.I.J. Van Dijke, G.D. Couples, Z. Jiang, J. Ma, K.S. Sorbie, J. Crawford, I. Young, X. Zhang, 3D stochastic modelling of heterogeneous porous media – applications to reservoir rocks, *Transp. Porous Media* 65 (2006) 443–467.
- [34] H. Okabe, M.J. Blunt, Prediction of permeability for porous media reconstructed using multiple-point statistics, *Phys. Rev. E* 70 (2004) 066135.
- [35] H. Okabe, M. Blunt, Pore space reconstruction of vuggy carbonates using microtomography and multiple-point statistics, *Water Resour. Res.* 43 (2007).
- [36] L. Mosser, O. Dubrule, M.J. Blunt, Stochastic Reconstruction of an Oolitic Limestone by Generative Adversarial Networks, *Transport in Porous Media*, 2018.
- [37] Y. Wang, C.H. Arns, S.S. Rahman, J.-Y. Arns, Porous structure reconstruction using convolutional neural networks, *Math. Geosci.* 50 (2018) 781–799.
- [38] S. Bakke, P.-E. Øren, 3-D pore-scale modelling of sandstones and flow simulations in the pore networks, *SPE J.* 2 (1997) 136–149.
- [39] P. Abrahamsen, *A Review of Gaussian Random Fields and Correlation Functions*, 1997.
- [40] M.Y. Joshi, *A Class of Stochastic Models for Porous Media*, Chemical and Petroleum Engineering, University of Kansas, 1974.
- [41] P.M. Adler, 7 - Reconstructed porous media, in: P.M. Adler (Ed.), *Porous Media*, Butterworth-Heinemann, Boston, 1992, pp. 503–538.
- [42] A.P. Roberts, E.J. Garboczi, Elastic properties of a tungsten–silver composite by reconstruction and computation, *J. Mech. Phys. Solids* 47 (1999) 2029–2055.
- [43] S.B. Strebelle, A.G. Journel, Reservoir modeling using multiple-point statistics, in: *SPE Annual Technical Conference and Exhibition*, New Orleans, Louisiana, 2001.
- [44] L.M. Pant, *Stochastic Characterization and Reconstruction of Porous Media*, Department of Mechanical Engineering, University of Alberta, 2016.
- [45] S. Torquato, *Random Heterogeneous Materials: Microstructure and Macroscopic Properties*, Springer, New York, USA, 2000.
- [46] S. Geman, D. Geman, Stochastic relaxation, Gibbs distributions, and the Bayesian restoration of images, *IEEE Trans. Pattern Anal. Mach. Intell.* 6 (1984) 721–741.
- [47] L. Ingber, Simulated annealing: practice versus theory, *Math. Comput. Model.* 18 (1993) 29–57.
- [48] G. Dueck, New optimization heuristics, *J. Comput. Phys.* 104 (1993) 86–92.
- [49] A.R.N. Metropolis, M. Rosenbluth, A. Teller, Equation of state calculations by fast computing machines, *J. Chem. Phys.* 21 (1953) 6.
- [50] G. Dueck, T. Scheuer, Threshold accepting: a general purpose optimization algorithm appearing superior to simulated annealing, *J. Comput. Phys.* 90 (1990) 161–175.
- [51] L.M. Pant, S.K. Mitra, M. Secanell, Multigrid hierarchical simulated annealing method for reconstructing heterogeneous media, *Phys. Rev. E* 92 (2015) 063303.
- [52] S. Geman, D. Geman, Stochastic relaxation, Gibbs distributions, and the Bayesian restoration of images, *IEEE Trans. Pattern Anal. Mach. Intell.* PAMI-6 (1984) 721–741.
- [53] W. Qian, D.M. Titterton, Multidimensional Markov chain models for image textures, *J. R. Stat. Soc., Ser. B, Methodol.* 53 (1991) 661–674.
- [54] K. Wu, N. Nunan, J.W. Crawford, I.M. Young, K. Ritz, An efficient Markov chain model for the simulation of heterogeneous soil structure, *Soil Sci. Soc. Am. J.* 68 (2004) 6.
- [55] F.B. Guardiano, R.M. Srivastava, Multivariate geostatistics: beyond bivariate moments, in: A. Soares (Ed.), *Geostatistics Tróia '92*, vol. 1, Springer Netherlands, Dordrecht, 1993, pp. 133–144.

- [56] A.S. Høyer, G. Vignoli, T. Mejer Hansen, L.T. Vu, D.A. Keefer, F. Jørgensen, Multiple-point statistical simulation for hydrogeological models: 3D training image development and conditioning strategies, *Hydrol. Earth Syst. Sci. Discuss.* 2016 (2016) 1–29.
- [57] S. Zhongkui, L. Peijun, A comparison of multiple-point statistics and two-point statistics for spectral-spatial land cover classification, in: 2016 4th International Workshop on Earth Observation and Remote Sensing Applications, EORSA, 2016, pp. 255–259.
- [58] A. Comunian, P. Renard, J. Straubhaar, 3D multiple-point statistics simulation using 2D training images, *Comput. Geosci.* 40 (2012) 49–65.
- [59] T.L. Chugunova, L.Y. Hu, Multiple-point simulations constrained by continuous auxiliary data, *Math. Geosci.* 40 (2008) 133–146.
- [60] Y. Liu, Using the Snesim program for multiple-point statistical simulation, *Comput. Geosci.* 32 (2006) 1544–1563.
- [61] S. Strebelle, N. Remy, Post-processing of multiple-point geostatistical models to improve reproduction of training patterns, in: O. Leuangthong, C.V. Deutsch (Eds.), *Geostatistics Banff 2004*, Springer Netherlands, Dordrecht, 2005, pp. 979–988.
- [62] S. Strebelle, T. Zhang, Non-stationary multiple-point geostatistical models, in: O. Leuangthong, C.V. Deutsch (Eds.), *Geostatistics Banff 2004*, Springer Netherlands, Dordrecht, 2005, pp. 235–244.
- [63] M. Le Coz, P. Genthon, P.M. Adler, Multiple-point statistics for modeling facies heterogeneities in a porous medium: the Komadugu-Yobe alluvium, Lake Chad Basin, *Math. Geosci.* 43 (2011) 861.
- [64] H. Okabe, M.J. Blunt, Pore space reconstruction using multiple-point statistics, *J. Pet. Sci. Eng.* 46 (2005) 121–137.
- [65] J.G. Hernandez, A Stochastic Approach to the Simulation of Block Conductivity Fields Conditioned upon Data Measured at a Smaller Scale, University of California-Department of Earth Sciences, 1991.
- [66] T.T. Tran, Improving variogram reproduction on dense simulation grids, *Comput. Geosci.* 20 (1994) 1161–1168.
- [67] S. Strebelle, K. Payrazyan, J. Caers, Modeling of a Deepwater Turbidite Reservoir Conditional to Seismic Data Using Principal Component Analysis and Multiple-Point Geostatistics, 2003.
- [68] S. Strebelle, Conditional simulation of complex geological structures using multiple-point statistics, *Math. Geol.* 34 (2002) 21.
- [69] L.Y. Hu, T. Chugunova, Multiple-point geostatistics for modeling subsurface heterogeneity: a comprehensive review, *Water Resour. Res.* 44 (2008).
- [70] A. Hajizadeh, A. Safekordi, F.A. Farhadpour, A multiple-point statistics algorithm for 3D pore space reconstruction from 2D images, *Adv. Water Resour.* 34 (2011) 1256–1267.
- [71] S. Strebelle, *Sequential Simulation Drawing Structures from Training Images*, Stanford University, 2000.
- [72] Y. Wu, C. Lin, L. Ren, W. Yan, S. An, B. Chen, Y. Wang, X. Zhang, C. You, Y. Zhang, Reconstruction of 3D porous media using multiple-point statistics based on a 3D training image, *J. Nat. Gas Sci. Eng.* 51 (2018) 129–140.
- [73] M.E. Naraghi, 3-D reconstruction of porous media and rock characterization, in: SPE Annual Technical Conference and Exhibition, Society of Petroleum Engineers, Dubai, UAE, 2016.
- [74] P. Tahmasebi, A. Hezarkhani, M. Sahimi, Multiple-point geostatistical modeling based on the cross-correlation functions, *Comput. Geosci.* 16 (2012) 779–797.
- [75] C. Daly, Higher order models using entropy, Markov random fields and sequential simulation, in: O. Leuangthong, C.V. Deutsch (Eds.), *Geostatistics Banff 2004*, Springer Netherlands, Dordrecht, 2005, pp. 215–224.
- [76] L. Feyen, J. Caers, Quantifying geological uncertainty for flow and transport modeling in multi-modal heterogeneous formations, *Adv. Water Resour.* 29 (2006) 912–929.
- [77] G.B. Arpat, J. Caers, A multiple-scale, pattern-based approach to sequential simulation, in: O. Leuangthong, C.V. Deutsch (Eds.), *Geostatistics Banff 2004*, Springer, 2005, pp. 255–264.
- [78] P. Tahmasebi, F. Javadpour, M. Sahimi, Three-dimensional stochastic characterization of shale SEM images, *Transp. Porous Media* 110 (2015) 521–531.
- [79] T. Zhang, P. Switzer, A. Journel, Filter-based classification of training image patterns for spatial simulation, *Math. Geol.* 38 (2006) 63–80.
- [80] Y. Wang, S.S. Rahman, C.H. Arns, Super resolution reconstruction of  $\mu$ -CT image of rock sample using neighbour embedding algorithm, *Phys. A, Stat. Mech. Appl.* 493 (2017) 177–188.
- [81] H. Okabe, M.J. Blunt, Pore space reconstruction of vuggy carbonates using microtomography and multiple-point statistics, *Water Resour. Res.* 43 (2007).
- [82] P. Tahmasebi, F. Javadpour, M. Sahimi, M. Piri, Multiscale study for stochastic characterization of shale samples, *Adv. Water Resour.* 89 (2016) 91–103.
- [83] P. Tahmasebi, M. Sahimi, J.E. Andrade, Image-based modeling of granular porous media, *Geophys. Res. Lett.* 44 (2017) 4738–4746.
- [84] P. Tahmasebi, F. Javadpour, M. Sahimi, Stochastic shale permeability matching: three-dimensional characterization and modeling, *Int. J. Coal Geol.* 165 (2016) 231–242.
- [85] L. Mosser, O. Dubrule, M.J. Blunt, Reconstruction of three-dimensional porous media using generative adversarial neural networks, *Phys. Rev. E* 96 (2017) 043309.
- [86] Y. LeCun, B. Boser, J.S. Denker, D. Henderson, R.E. Howard, W. Hubbard, L.D. Jackel, Backpropagation applied to handwritten zip code recognition, *Neural Comput.* 1 (1989) 541–551.
- [87] A. Krizhevsky, I. Sutskever, G.E. Hinton, ImageNet classification with deep convolutional neural networks, *Commun. ACM* 60 (2017) 84–90.
- [88] J. Deng, W. Dong, R. Socher, L.J. Li, L. Kai, F.-F. Li, ImageNet: a large-scale hierarchical image database, in: 2009 IEEE Conference on Computer Vision and Pattern Recognition, 2009, pp. 248–255.
- [89] Y. Guo, Y. Liu, A. Oerlemans, S. Lao, S. Wu, M.S. Lew, Deep learning for visual understanding: a review, *Neurocomputing* 187 (2016) 27–48.
- [90] D. Chaoben, G. Shesheng, Multi-focus image fusion with the all convolutional neural network, *Optoelectron. Lett.* 14 (2018) 71–75.
- [91] J.T. Springenberg, A. Dosovitskiy, T. Brox, M. Riedmiller, Striving for simplicity: the all convolutional net, arXiv e-prints, arXiv:1412.6806 [cs.LG], 2014.
- [92] Y. LeCun, Y. Bengio, G. Hinton, Deep learning, *Nature* 521 (2015) 436–444.